narrower second-order resonances that are associated with double and triple occupancy, respectively.

28. S. Fölling et al., Nature 448, 1029–1032 (2007).
29. F. Meinert et al., Science 344, 1259–1262 (2014).
30. Materials and methods are available as supplementary materials on Science Online.
31. I. B. Spielman, W. D. Phillips, J. V. Porto, Phys. Rev. Lett. 100, 120402 (2008).

QUANTUM GASES

Observation of isolated monopoles in a quantum field

M. W. Ray,[1]* E. Ruokokoski,[2] K. Tiurev,[2] M. Möttönen,[2,3]† D. S. Hall[1]

Topological defects play important roles throughout nature, appearing in contexts as diverse as cosmology, particle physics, superfluidity, liquid crystals, and metallurgy. Point defects can arise naturally as magnetic monopoles resulting from symmetry breaking in grand unified theories. We devised an experiment to create and detect quantum mechanical analogs of such monopoles in a spin-1 Bose-Einstein condensate. The defects, which were stable on the time scale of our experiments, were identified from spin-resolved images of the condensate density profile that exhibit a characteristic dependence on the choice of quantization axis. Our observations lay the foundation for experimental studies of the dynamics and stability of topological point defects in quantum systems.

Two structures are topologically equivalent if they can be continuously transformed into one another (1, 2), such as the letters O and P. Topological defects exist in a physical system if its state is not topologically equivalent to its ground state. Such defects can decay or disappear only as a result of globally nontrivial transformations, rendering them long-lived and ubiquitous in the universe.

Line defects are among the most common topological structures. In classical physics, for example, dislocations in a crystal lattice (3) can determine the strength and hardness of materials. In quantum physics, a line defect in a complex-valued order parameter is accompanied by a phase winding of an integer multiple of 2π. These quantized vortices are regarded as the hallmark of superfluidity (4, 5) and constitute a versatile tool in the study of quantum physics. In contrast, the roles played by point defects in three-dimensional superfluids and superconductors remain less explored experimentally, although related objects such as skyrmion solitons and boojums at domain interfaces have been observed (6–9).

Homotopy theory (2, 10) is a mathematical tool that classifies topological point defects according to the behavior of the order parameter on closed surfaces. Evaluation of the second homotopy group reveals whether point defects can occur. Nematic liquid crystals (11) and colloids (12) are examples of classical systems for which the second homotopy group is nontrivial and point defects have been observed [see also (13)]. Quantum systems described by multidimensional fields are also predicted to support point defects as stable elementary particles (2). The magnetic monopole (14, 15) that emerges under broken symmetry in grand unified theories (16) is one such example.

The polar phase of a spin-1 Bose-Einstein condensate (BEC) permits the existence of topological point defects in the quantum mechanical order parameter (17, 18). Although these defects are not elementary particles, they are analogous quantum objects often referred to as monopoles.

In our experiments, we create a topological point defect in the spin-1 order parameter of an ^{87}Rb BEC using a method originally suggested in (19) and used to create Dirac monopoles in a fer-romagnetic BEC in (20) [see related work in (21)]. The key technical difference relative to (20) is that the condensate is initialized in its polar phase. This seemingly minor modification leads to a topological excitation with properties that are fundamentally different from those of the recently observed Dirac monopole. The Dirac monopole is not a pointlike topological defect in the order parameter, as the second homotopy group of the ferromagnetic phase contains only the identity element (22). Consequently, Dirac monopoles are attached to at least one terminating nodal line (23), which renders the energetics and dynamics of the excitation similar to those of vortices. No such nodal line is attached to the point defect structure we create here in the order parameter field, and hence we refer to it as an isolated monopole.

A spin-1 condensate can be described by the order parameter

$$\Phi(\mathbf{r}) = \sqrt{n(\mathbf{r})}\exp[i\phi(\mathbf{r})]\zeta(\mathbf{r}) \qquad (1)$$

where n is the particle density, ϕ is the scalar phase, and the spinor is represented by a normalized complex-valued vector $\zeta = (\zeta_{+1}\ \zeta_0\ \zeta_{-1})^T$. Here, $\zeta_m = \langle m|\zeta\rangle$ is the mth spinor component along the quantization axis z. The most general polar order parameter, for which the local spin vanishes, is given by

$$\Phi = \frac{\sqrt{n}\,\exp(i\phi)}{\sqrt{2}}\begin{pmatrix} -\exp(-i\alpha)\sin\beta \\ \sqrt{2}\cos\beta \\ \exp(i\alpha)\sin\beta \end{pmatrix}$$

$$= \frac{\sqrt{n}\,\exp(i\phi)}{\sqrt{2}}\begin{pmatrix} -d_x + id_y \\ \sqrt{2}d_z \\ d_x + id_y \end{pmatrix} \qquad (2)$$

where the Euler angles $\beta(\mathbf{r})$ and $\alpha(\mathbf{r})$ refer to the spin rotation of a spinor $(0\ 1\ 0)^T$ about the y and z axes, respectively, and $\hat{\mathbf{d}}$ is a three-dimensional

[1]Department of Physics and Astronomy, Amherst College, Amherst, MA 01002, USA. [2]QCD Labs, COMP Centre of Excellence, Department of Applied Physics, Aalto University, FI-00076 Aalto, Finland. [3]Low Temperature Laboratory (OVLL), Aalto University, FI-00076 Aalto, Finland.
*Present address: Department of Physics and Astronomy, Union College, Schenectady, NY 12308, USA. †Corresponding author. E-mail: mikko.mottonen@aalto.fi
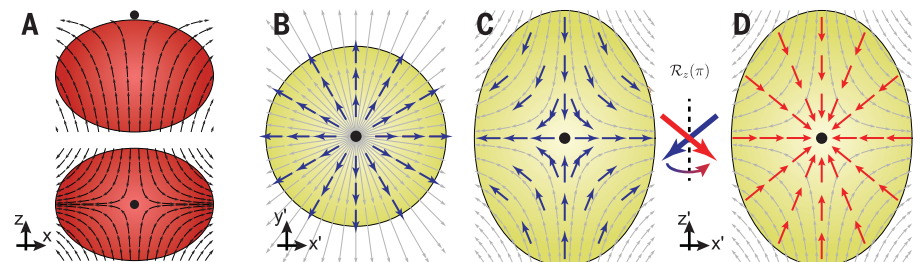
Fig. 1. Schematic representation of the experiment. (**A**) Magnetic field lines as B_z is decreased. The zero point of the magnetic field is shown as a black dot. (**B** to **D**) Cross sections through the condensate in the $x'y'$ plane (B) and in the $x'z'$ plane (C) showing the nematic vector field (thick arrows) defining our isolated monopole structure, which is related to the hedgehog monopole structure (D) by a rotation of π about the z' axis, $\mathcal{R}_z(\pi)$. The primed coordinates are defined as $x' = x$, $y' = y$, and $z' = 2z$; the gray arrows depict magnetic field lines.

real-valued unit vector field known as the nematic vector. Equation 2 shows that the polar spin-1 condensate is simply described by the mean-field order parameter

$$\Psi(\mathbf{r}) = \sqrt{n(\mathbf{r})}\exp[i\phi(\mathbf{r})]\hat{\mathbf{d}}(\mathbf{r}) \qquad (3)$$

with its topological properties determined by the factor $\exp[i\phi(\mathbf{r})]\hat{\mathbf{d}}(\mathbf{r})$ (24). Note that any unitary spin rotation imposed on the order parameter in Eq. 2 corresponds to an identical rotation of $\hat{\mathbf{d}}$. Thus, the nematic vector $\hat{\mathbf{d}}$ follows adiabatic changes in the external magnetic field, much as the direction of the spin follows the field in the ferromagnetic case.

The initial atom number in the optically trapped ^{87}Rb BEC is $N \approx 2.1 \times 10^5$ with calculated radial and axial Thomas-Fermi radii $R = 7.2$ μm and $Z = 5.4$ μm, respectively, and corresponding optical trapping frequencies $\omega_r \approx 2\pi \times 124$ Hz and $\omega_z \approx 2\pi \times 164$ Hz, respectively. The creation process begins with $\hat{\mathbf{d}}$ aligned with a uniform magnetic field $\mathbf{B}_b(t) = B_x(t)\hat{\mathbf{x}} + B_y(t)\hat{\mathbf{y}} + B_z(t)\hat{\mathbf{z}}$

(24). We use $\mathbf{B}_b(t) = B_z(t)\hat{\mathbf{z}}$ here, but the experimental results are independent of the choice of direction. A quadrupole magnetic field $\mathbf{B}_q(\mathbf{r}) = b_q(x\hat{\mathbf{x}} + y\hat{\mathbf{y}} - 2z\hat{\mathbf{z}})$ of strength $b_q = 3.7$ G/cm is then introduced; the zero point

$$\mathbf{r}_0(t) = \frac{-B_x(t)\hat{\mathbf{x}} - B_y(t)\hat{\mathbf{y}} + \frac{B_z(t)\hat{\mathbf{z}}}{2}}{b_q} \qquad (4)$$

of the total magnetic field $\mathbf{B}(\mathbf{r},t) = \mathbf{B}_q(\mathbf{r}) + \mathbf{B}_b(t)$ is initially located well outside the condensate. We then change $\mathbf{B}_b$ until $\mathbf{r}_0$ lies near the center of the condensate (Fig. 1A). This "creation ramp" is carried out nearly adiabatically ($dB_z/dt = -0.25$ G/s)—that is, $\hat{\mathbf{d}}(\mathbf{r},t) \approx \hat{\mathbf{B}}(\mathbf{r},t)$—thereby creating the isolated monopole structure in the order parameter field shown in Fig. 1, B and C. Nonadiabatic excitations and spin-exchange collisions are measured to be relatively small (~10%) for the experimental parameter values used here.

To select a quantization axis for imaging the monopole structure, we apply a "projection ramp" in which the magnetic bias field is rapidly in-

creased to $|\mathbf{B}_b|/b_q \gg \{R, Z\}$ along a direction of our choice, $\hat{\mathbf{z}}_p$, leaving the nematic vector essentially unchanged. Subsequently, the spinor components quantized along this axis, $\langle m_p|\zeta\rangle$, are spatially separated and imaged in both the vertical ($\hat{\mathbf{z}}$) and horizontal ($\hat{\mathbf{y}}$) directions (24). In Fig. 2, A and D, we show the corresponding experimentally obtained particle densities in the simple case $\hat{\mathbf{z}}_p = -\hat{\mathbf{z}}$. The theory [Eq. 2 with $\hat{\mathbf{d}}(\mathbf{r},t) = \hat{\mathbf{B}}_q(\mathbf{r})$] predicts hollow-core vortices of opposite unit circulations in the $m = \pm 1$ components along z, in agreement with the observed density "holes" in Fig. 2D. The unit phase winding and the opposite circulations of the two vortices are experimentally confirmed using interferometric techniques (24) (figs. S1 and S2). Furthermore, the data in Fig. 2, A and C, are in qualitative agreement with Eq. 2 because the particle density in the $m = 0$ component $n|\zeta_0|^2 \propto d_z^2$ vanishes in the $z = 0$ plane, and the other two components $n|\zeta_{\pm 1}|^2 \propto d_x^2 + d_y^2$ accumulate in its vicinity. This agreement constitutes the primary evidence for the existence of the monopole.

We modeled the experimental creation and imaging process numerically by solving the full three-dimensional dynamics of the mean-field spinor order parameter from the spin-1 Gross-Pitaevskii equation (19). Figures 2 and 3 show one-to-one comparisons of the numerically obtained particle density distributions to the experimental results without any free parameters. The good quantitative agreement between the simulations and the experiments reinforces the congruence between the experiments and the results of the analytic theory, thereby providing complementary evidence for the realization of an isolated monopole structure in the order parameter. Discrepancies between the numerical and experimental results—for example, the density peak in the $m = 0$ component in Fig. 2F—may arise from the experimental noise and the choice of imaging technique that are not taken fully into account in the simulations (24).

Particle densities identical to those shown in Fig. 2 for our isolated monopole are expected for the topologically equivalent hedgehog monopole structure shown in Fig. 1D, as the only difference between the spinors of the two configurations is the sign of the $m = \pm 1$ components (see Eq. 2 and Fig. 1, C and D). In fact, after the projection ramp $\hat{\mathbf{z}}_p = \pm\hat{\mathbf{z}}$, the order parameter oscillates between the two configurations because of the 350-kHz Larmor precession of the nematic vector about $\hat{\mathbf{z}}$. Because the other condensate dynamics occur on much longer time scales, the experiment also accurately produces the hedgehog monopole, as confirmed by the numerical simulations shown in fig. S3.

One characteristic feature of a quantum mechanical point defect is that arbitrary rotations of a properly chosen coordinate system, $\mathcal{D}$, can be compensated by rotations in the order parameter space, $\hat{\mathcal{D}}$, and vice versa. We study whether the created point defect has this property by imposing a spin rotation $\hat{\mathcal{D}}_p$ on the spin state of the defect $|\zeta\rangle$ such that we choose the direction of the projection ramp, $\hat{\mathbf{z}}_p$, defined by

Fig. 2. Experiment compared to numerical simulations following a projection ramp along −z. (**A** and **D**) Experimentally obtained images of the condensate taken along the horizontal (y) axis (A) and the vertical (z) axis (D). (**B** and **E**) Results of the corresponding numerical simulations. In each panel, the top image gives a false-color composite, in which the color intensity represents the particle density of each spinor component integrated along the respective imaging axis. The lower three sets of images show the densities for the individual components. (**C** and **F**) Quantitative comparison of experimental (solid lines) and simulated (dashed lines) column density, $\tilde{n}$, for cross sections. The field of view is 288 μm × 288 μm for images along the horizontal axis and 219 μm × 219 μm for those along the vertical axis. The peak column density in all images is $\tilde{n}_p = 12.9 \times 10^8$ cm^{-2}. Color and intensity scales are shown at bottom of figure.
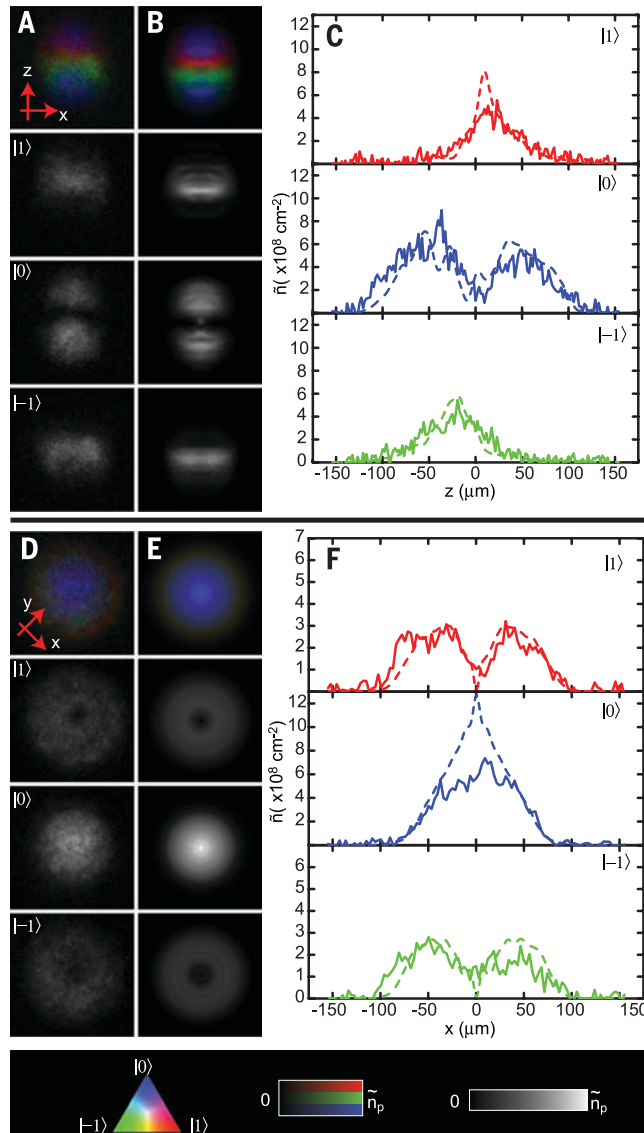
the coordinate rotation $(x_p, y_p, z_p) = \mathcal{D}_p^{-1}(x, y, z)$. The projection of the original spinor onto the new z_p-quantized basis is equal to the projection of the rotated spinor onto the z-quantized basis:

$$\langle m_p|\zeta\rangle = \langle m_p|\hat{\mathcal{D}}_p^\dagger \hat{\mathcal{D}}_p|\zeta\rangle = \langle m|\hat{\mathcal{D}}_p|\zeta\rangle \quad (5)$$

Thus, the rotational compensation property given above demands that there exists a rotation $\mathcal{D}_v$ into a new coordinate system $(x_v, y_v, z_v) = \mathcal{D}_v(x, y, z)$ such that Eq. 2, with (x, y, z) replaced by (x_v, y_v, z_v), yields the observed spinor components. Below, we analytically find the new coordinate system for both the hedgehog monopole and our isolated monopole in the case of an arbitrary projection axis, and show matching experimental observations.

The hedgehog monopole is characterized by the nematic vector $\hat{\mathbf{d}}_h = -\hat{\mathbf{r}}'$, where the primed coordinates are defined as $(x', y', z') = (x, y, 2z)$. Because the radial vectors in any two rotated coordinate systems coincide, $\hat{\mathbf{r}}'(x'_p, y'_p, z'_p) = \hat{\mathbf{r}}'_p(x'_p, y'_p, z'_p)$, we can choose $(x'_v, y'_v, z'_v) = (x'_p, y'_p, z'_p)$ (i.e., $\mathcal{D}_v = \mathcal{D}_p^{-1}$). Together with Eq. 2, this shows that the vortices in the $m_p = \pm 1$ components of the hedgehog configuration always align with the projection axis $\hat{\mathbf{z}}_p$. To find how the vortices will be oriented in the case of our isolated monopole, we make use of the property that the hedgehog monopole is obtained from the isolated monopole configuration by a continuous π-rotation about the z axis (Fig. 1, C and D); that is, $\hat{\mathcal{R}}_z(\pi)|\zeta_m\rangle = |\zeta_h\rangle$ and $\mathcal{R}_z(\pi)\hat{\mathbf{d}}_m = \hat{\mathbf{d}}_h$. By writing the observed spinor component as

$$\begin{aligned}\langle m_p|\zeta_m\rangle &= \langle m_p|\hat{\mathcal{R}}_z(\pi)^\dagger \hat{\mathcal{R}}_z(\pi)|\zeta_m\rangle \\ &= [\langle m_p|\hat{\mathcal{R}}_z(\pi)^\dagger]|\zeta_h\rangle\end{aligned} \quad (6)$$

we find that a proper choice of the new coordinate system is $(x_v, y_v, z_v) = \mathcal{R}_z(\pi)(x_p, y_p, z_p)$. Thus, the vortices are aligned with $\hat{\mathbf{z}}_v = \mathcal{R}_z(\pi)\hat{\mathbf{z}}_p$.

The isolated monopole (Fig. 1, B and C) is topologically equivalent to the hedgehog structure (Fig. 1D) and has the same topological charge and stability properties. However, the fact that the projection axis and the vortex axis are not always aligned makes the isolated monopole an ideal object to demonstrate that the observed vortices are not technical artifacts of the projection ramp. The corresponding experimental results are shown in Fig. 4. In agreement with the result $\hat{\mathbf{z}}_v = \mathcal{R}_z(\pi)\hat{\mathbf{z}}_p$ derived above, we observe that the two axes, $\hat{\mathbf{z}}_v$ and $\hat{\mathbf{z}}_p$, are parallel when they lie in the xy plane (Fig. 4A) and rotate in opposite directions in the xz plane (Fig. 4B).

Both monopole structures are expected to exhibit an instability toward a formation of a vortex ring (25). Although this and other instabilities (26, 27) occur slowly enough not to disturb the creation and imaging process (24), observation of the resulting decay dynamics and implementation of a system in their absence are interesting research directions. Furthermore, studies of the interaction between monopoles and other topological defects, such as domain walls and skyrmions (7), may yield additional insights into high-energy physics and cosmology (28). A related goal is to

create a topological point defect that also generates the synthetic magnetic field of a monopole, thereby combining the scenarios of Dirac (23), 't Hooft (14), and Polyakov (15). Finally, the observation of non-Abelian monopoles (29, 30) remains an important goal.
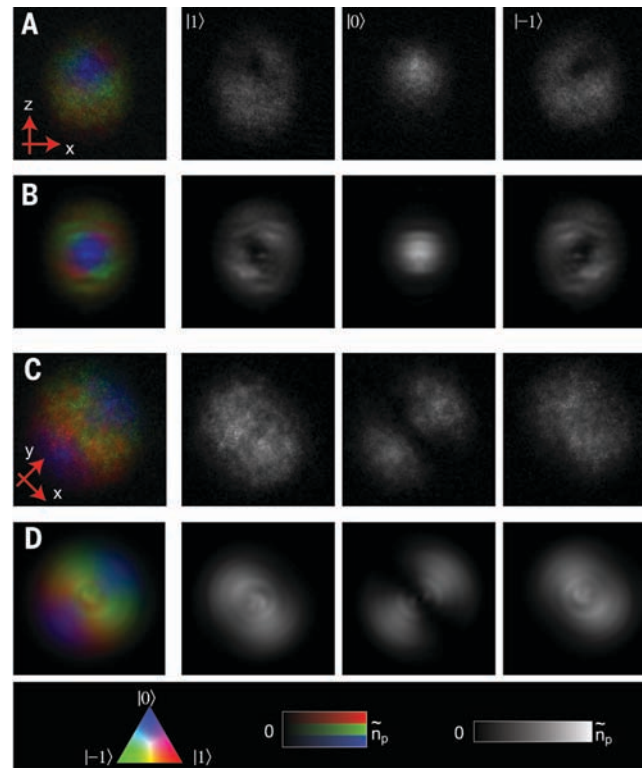

Fig. 3. Experiment compared to numerical simulations following a projection ramp along −y. (**A**) Experimentally obtained images of the condensate taken along the horizontal (y) axis. (**B**) Results of the corresponding numerical simulations. See Fig. 2 for further description. (**C** and **D**) As above, but for images taken along the vertical (z) axis. The field of view is 288 μm × 288 μm in (A) and (B), 219 μm × 219 μm in (C) and (D). The peak column density is $\tilde{n}_p = 12.9 \times 10^8 \text{ cm}^{-2}$.
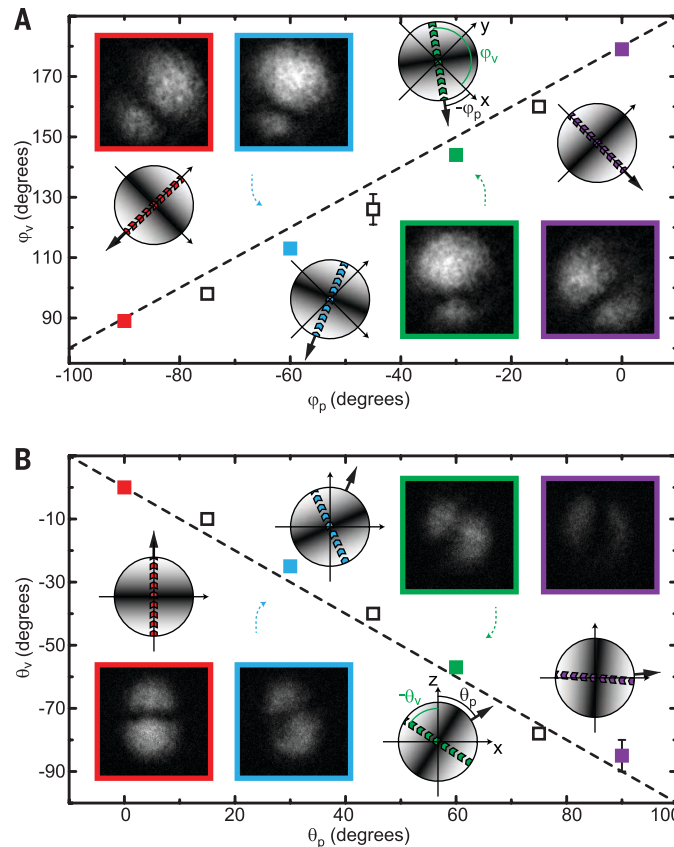

Fig. 4. Experimental results for different choices of the projection axis. (**A**) The angle of the vortices in the $|m = \pm 1\rangle$ states, φ_v, resulting from projections in the xy plane with azimuthal angle φ_p. Condensates are imaged along the z axis and φ_v is extracted from the alignment of the density profile in the $|m = 0\rangle$ state, as shown in the insets (see also figs. S4 to S7). Typical uncertainties are indicated by the error bars shown. The dashed line shows the theoretical result. The black arrows in the insets show the projection axes, z_p, and the chevrons show the expected orientation of the vortex axes, z_v. (**B**) Same as (A) but for angles θ_v resulting from projections in the xz plane with polar angle θ_p and imaging axis y.

REFERENCES AND NOTES

1. N. D. Mermin, *Rev. Mod. Phys.* **51**, 591–648 (1979).
2. M. Nakahara, *Geometry, Topology and Physics* (Taylor & Francis, Boca Raton, FL, 2003).
3. N. W. Ashcroft, N. D. Mermin, *Solid State Physics* (Harcourt, Orlando, FL, 1976).
4. R. J. Donnelly, *Quantized Vortices in Helium II* (Cambridge Univ. Press, Cambridge, 1991).
5. A. L. Fetter, *Rev. Mod. Phys.* **81**, 647–691 (2009).
6. J. Y. Choi, W. J. Kwon, Y. I. Shin, *Phys. Rev. Lett.* **108**, 035301 (2012).
7. P. Milde *et al.*, *Science* **340**, 1076–1080 (2013).
8. R. Blaauwgeers *et al.*, *Nature* **404**, 471–473 (2000).
9. R. Blaauwgeers *et al.*, *Phys. Rev. Lett.* **89**, 155301 (2002).
10. G. Toulouse, M. Kléman, *J. Phys. Lett.* **37**, 149–151 (1976).
11. I. Chuang, R. Durrer, N. Turok, B. Yurke, *Science* **251**, 1336–1342 (1991).
12. B. Senyuk *et al.*, *Nature* **493**, 200–205 (2013).
13. S. T. Bramwell *et al.*, *Nature* **461**, 956–959 (2009).
14. G. 't Hooft, *Nucl. Phys. B* **79**, 276–284 (1974).
15. A. M. Polyakov, *JETP Lett.* **20**, 194 (1974).
16. J. Preskill, *Annu. Rev. Nucl. Part. Sci.* **34**, 461–530 (1984).
17. H. T. C. Stoof, E. Vliegen, U. Al Khawaja, *Phys. Rev. Lett.* **87**, 120407 (2001).
18. F. Zhou, *Int. J. Mod. Phys. B* **17**, 2643–2698 (2003).
19. V. Pietilä, M. Möttönen, *Phys. Rev. Lett.* **103**, 030401 (2009).
20. M. W. Ray, E. Ruokokoski, S. Kandel, M. Möttönen, D. S. Hall, *Nature* **505**, 657–660 (2014).
21. J. Y. Choi, S. Kang, S. W. Seo, W. J. Kwon, Y. I. Shin, *Phys. Rev. Lett.* **111**, 245301 (2013).
22. Y. Kawaguchi, M. Ueda, *Phys. Rep.* **520**, 253–381 (2012).
23. P. A. M. Dirac, *Proc. R. Soc. London Ser. A* **133**, 60–72 (1931).
24. See supplementary materials on *Science* Online.
25. J. Ruostekoski, J. R. Anglin, *Phys. Rev. Lett.* **91**, 190402 (2003).
26. W. Zhang, D. L. Zhou, M.-S. Chang, M. S. Chapman, L. You, *Phys. Rev. Lett.* **95**, 180403 (2005).
27. L. E. Sadler, J. M. Higbie, S. R. Leslie, M. Vengalattore, D. M. Stamper-Kurn, *Nature* **443**, 312–315 (2006).
28. O. Borgh, J. Ruostekoski, *Phys. Rev. Lett.* **109**, 015302 (2012).
29. J. Ruseckas, G. Juzeliūnas, P. Ohberg, M. Fleischhauer, *Phys. Rev. Lett.* **95**, 010404 (2005).
30. V. Pietilä, M. Möttönen, *Phys. Rev. Lett.* **102**, 080403 (2009).

SUPPLEMENTARY MATERIALS

www.sciencemag.org/content/348/6234/544/suppl/DC1
Materials and Methods
Supplementary Text
Figs. S1 to S11
Reference (*31*)

FERROELECTRICS

Observation of a periodic array of flux-closure quadrants in strained ferroelectric PbTiO3 films

Y. L. Tang,[1]* Y. L. Zhu,[1]* X. L. Ma,[1]† A. Y. Borisevich,[2] A. N. Morozovska,[3] E. A. Eliseev,[4] W. Y. Wang,[1] Y. J. Wang,[1] Y. B. Xu,[1] Z. D. Zhang,[1] S. J. Pennycook[5,6]

Nanoscale ferroelectrics are expected to exhibit various exotic domain configurations, such as the full flux-closure pattern that is well known in ferromagnetic materials. Here we observe not only the atomic morphology of the flux-closure quadrant but also a periodic array of flux closures in ferroelectric PbTiO3 films, mediated by tensile strain on a GdScO3 substrate. Using aberration-corrected scanning transmission electron microscopy, we directly visualize an alternating array of clockwise and counterclockwise flux closures, whose periodicity depends on the PbTiO3 film thickness. In the vicinity of the core, the strain is sufficient to rupture the lattice, with strain gradients up to 10^9 per meter. Engineering strain at the nanoscale may facilitate the development of nanoscale ferroelectric devices.

Atomic-scale information is of critical importance for understanding intrinsic characteristics of advanced functional materials such as ferroelectrics, magnets, superconductors, and catalysts. For example, it is often the small deviations from symmetry in atom positions and the resultant strains that allow ferroelectric oxides, used in computer memory chips, to store charge and information or to resonate with magnets as composite multiferroics. Ferroelectric crystals feature asymmetric or polar structures that are switchable under an external field, holding promise for random access memories, thin-film capacitors, and actuators (*1*). For integration into silicon chips, practical ferroelectric memories take the form of nanoscale films (*1*). Nanoscale ferroelectrics have been predicted to undergo unusual phase transitions and exhibit distinctive domain patterns, such as closure quadrants with closed head-tail dipole moments, known as flux closures (*2–7*). These flux-closure domains should be switchable and may give rise to an unusually high density of bits (*2*), and they can undergo vortex-polarization phase transformation (*6*). These domains are also predicted to be potentially useful as mechanical sensors and transducers (*7*). Similar domains are well known in ferromagnetic materials (*8–10*), and their topological properties and dynamics are under inves-

tigation (*9, 10*). However, in ferroelectric materials, particularly in tetragonal ferroelectrics, the coupling of polarization to spontaneous strain would be so pronounced that formation of a closure quadrant with its resultant severe disclination strains could be impossible (*11, 12*). Although closure quadrants were reported recently in tetragonal ferroelectric BaTiO3 (*13–16*), PbZr0.42Ti0.58O3 (*17*), and PZN-12PT (*18*), they are mostly composed of shape-conserving 90° stripe domains or twins within each quadrant to accommodate the disclination strains. In such cases, the closure quadrants may not always involve continuous dipole rotations, as have been observed directly in half of a closure quadrant in PbZr0.2Ti0.8O3 (*19*) and BiFeO3 (*20*) by aberration-correction transmission electron microscopy (TEM) or scanning TEM (STEM). The atomic-scale characterization based on STEM imaging has been validated to be capable of directly displaying ionic displacement maps (*19–24*), whereas approaches based on piezoresponse force microscopy are not able to do so because of lower spatial resolution (*11, 14–18, 25, 26*).

In this study, we have grown PbTiO3/SrTiO3 (PTO/STO) multilayer films on a GdScO3 substrate with a lattice parameter larger than the *a* value of PTO (*27*). Using aberration-corrected high-angle annular dark-field (HAADF) Z-contrast STEM imaging, we visualize, at the atomic scale, the existence of periodic twin-free flux-closure quadrants.

PbTiO3 has a tetragonal structure (Fig. 1A). Both the oxygen octahedra and the Ti^{4+} have displacements from the center of the Pb^{2+} tetragonal cell that give rise to the spontaneous polarization (Fig. 1, B and C). The shifts of Ti^{4+} (denoted as δ_{Ti} in Fig. 1B) can be used to determine the polarizations of PTO unit cells. In HAADF images, the Pb^{2+} columns appear as the brightest dots because the intensity of atom columns is approximately proportional to Z^2, where Z is the atomic number (*20, 21, 23, 24*). The Ti^{4+} columns show weaker contrast. The displacement vectors of Ti^{4+} (δ_{Ti}) relative to the center of mass of the

[1]Shenyang National Laboratory for Materials Science (SYNL), Institute of Metal Research, Chinese Academy of Sciences, Wenhua Road 72, 110016 Shenyang, China. [2]Oak Ridge National Laboratory, Materials Science and Technology Division, Oak Ridge, TN 37831-6071, USA. [3]Institute of Physics, National Academy of Sciences of Ukraine, 46 pr. Nauky, 03028 Kyiv, Ukraine. [4]Institute for Problems of Materials Sciences, National Academy of Sciences of Ukraine, 3 Krjijanovskogo, 03142 Kyiv, Ukraine. [5]Department of Materials Science and Engineering, University of Tennessee, Knoxville, TN 37996-2200, USA. [6]Department of Materials Science and Engineering, National University of Singapore, Singapore 117576, Singapore.
*These authors contributed equally to this work. †Corresponding author. E-mail: xlma@imr.ac.cn